


Effective reinforcement ratio of RC beams: Validation of modelling assumptions with high-resolution strain data

Journal Article**Author(s):**

Galkovski, Tena; [Mata Falcón, Jaime](#) ; Kaufmann, Walter

Publication date:

2022-06

Permanent link:

<https://doi.org/10.3929/ethz-b-000538266>

Rights / license:

[Creative Commons Attribution 4.0 International](#)

Originally published in:

Structural Concrete 23(3), <https://doi.org/10.1002/suco.202100739>

ARTICLE

Effective reinforcement ratio of RC beams: Validation of modelling assumptions with high-resolution strain data

Tena Galkovski  | Jaime Mata-Falcón  | Walter Kaufmann

Institute of Structural Engineering, ETH Zurich, Zurich, Switzerland

Correspondence

Tena Galkovski, Stefano-Francini-Platz
5, 8093 Zurich, Switzerland.

Email: galkovski@ibk.baug.ethz.ch

[Correction added on 20 April 2022, after first online publication: CSAL funding statement has been added.]

Abstract

Concrete tensile stresses influence the cracking behaviour and the stiffness of reinforced concrete (RC) members. Most design codes account for this tension stiffening effect using an effective reinforcement ratio. Although this ratio has a significant influence on the design of RC structures, its quantification is controversial in many cases, and typically relies on empirical geometry-based expressions. One main reason for this knowledge gap is that the area of concrete in tension can only be verified indirectly, for example, through crack widths and spacings and using a suitable mechanical model. This indirect validation is subject to considerable uncertainty as it depends on parameters that scatter (e.g., bond stresses and the concrete tensile strength), and further assumptions relating internal stresses to the applied loads are required. This article outlines

Abbreviations: A_c , Gross cross-sectional area of concrete; $A_{c,eff}$, Area of concrete in tension; A_s , Nominal steel area; D_{max} , Maximum aggregate size; E_c , Young's modulus of concrete; E_{cm} , Young's modulus of concrete (mean value); E_s , Young's modulus of reinforcement; E_{sh} , Strain hardening modulus of the reinforcement; E_I^{II} , Fully cracked elastic cross-sectional stiffness; F , Force; F_{ct} , Concrete tensile force; F_{cc} , Concrete compression force; $F_{cc,I}$, $F_{cc,II}$, Concrete compression force in the uncracked and cracked cross-sections I and II, respectively; F_s , Reinforcing bar force; $F_{s,I}$, $F_{s,II}$, Reinforcing bar force in the uncracked and cracked cross-sections I and II, respectively; V , Shear force; M , Bending moment; M_{cr} , Bending moment at cracking, cracking load; b , Cross-sectional width; c_{nom} , Concrete cover; d , Static height of the reinforcement; f_{ct} , Concrete tensile strength; f_{ctm} , Mean tensile strength; f_{cm} , Mean cylinder compressive strength; f_{su} , Tensile strength of reinforcing steel; f_{sy} , Yield strength of reinforcing steel in tension; f_{sy} , Yield strength of reinforcing steel's core in tension; h , Member height; $h_{c,eff}$, Height of the concrete area in tension; h_{ct} , Height of the concrete tensile zone subjected to f_{ct} (DC); $h_{ct,tr}$, Height of the concrete tensile zone with linearly decreasing tensile stresses (DC); u_x , Axial deformation; $u_{x,c}$, Axial deformations of the outermost concrete fiber in compression of a crack element; $u_{x,s}$, Axial deformations of reinforcement of a crack element; s_r , Real crack spacing; s_{rm} , Mean crack spacing; s_{r0} , Maximum crack spacing; w_{cr} , Crack width; x , x -coordinate; x_I , x_{II} , x -coordinate of the uncracked and cracked cross-sections I and II, respectively; x_c , Concrete compression zone height; $x_{c,I}$, $x_{c,II}$, Concrete compression zone height in the uncracked and cracked cross-sections I and II, respectively; y , y -coordinate; z , z -coordinate; z_c , Inner lever arm of forces; z_{cc} , Lever of the compressive concrete force; z_{ct} , Lever of the tensile concrete force; α_c , Modular ratio E_s/E_c ; ϵ_{cm} , Mean concrete strains; ϵ_{cc} , Concrete compressive strains; $\epsilon_{cc,I}$, $\epsilon_{cc,II}$, Concrete compressive strains of the outermost fiber in the uncracked and cracked cross-sections I and II, respectively; ϵ_{ct} , Concrete tensile strains; ϵ_{cu} , Ultimate concrete strain; ϵ_s , Steel strains; $\epsilon_{s,I}$, $\epsilon_{s,II}$, Steel strains in the uncracked and cracked cross-sections I and II, respectively; ϵ_{sh} , Hardening strain of the steel; ϵ_{sm} , Mean steel strains; ϵ_{sy} , Yield strain of the steel reinforcing bar; ϵ'_{sy} , Yield strain of the steel reinforcing bar's core; ϵ_x , Strains in x -direction; λ , Crack spacing parameter; ρ_{eff} , Effective reinforcement ratio; σ_s , Steel stresses; $\sigma_{s,I}$, $\sigma_{s,II}$, Steel stresses in the uncracked and cracked cross-sections I and II, respectively; τ_b , Bond shear stresses; τ_{bms} , Bond shear stresses according to the *fib* Model Code 2010; τ_{b0} , Bond shear stresses in the elastic steel phase (TCM); τ_{b1} , Bond shear stresses in the plastic steel phase (TCM); χ , Curvature; \emptyset , Nominal diameter of reinforcing bar; $\emptyset_{c,eff}$, Diameter of the maximum concrete area that can be activated by a bar (CSFM); \emptyset_{eff} , Effective reinforcing bar diameter.

Discussion on this paper must be submitted within two months of the print publication. The discussion will then be published in print, along with the authors' closure, if any, approximately nine months after the print publication.

This is an open access article under the terms of the [Creative Commons Attribution](https://creativecommons.org/licenses/by/4.0/) License, which permits use, distribution and reproduction in any medium, provided the original work is properly cited.

© 2022 The Authors. *Structural Concrete* published by John Wiley & Sons Ltd on behalf of International Federation for Structural Concrete.

how refined measurements of the reinforcing steel strains and the concrete deformations in the compression zone, combining distributed fibre optic sensing (DFOS) and digital image correlation (DIC), can be used in order to obtain a more reliable quantification of the parameters affecting tension stiffening and hence, the effective reinforcement ratio. Selected models are validated against experimental data of an RC beam tested under four-point bending, underlining the potential of DFOS and DIC as valuable tools for a better understanding of RC structures and the enhancement of mechanical models.

KEYWORDS

compatible stress field method, cross-sectional analysis, digital image correlation, distributed fibre optical sensors, effective area of concrete in tension, Euler-Bernoulli beam theory, plane strain assumption, pure bending, tension stiffening

1 | INTRODUCTION

The concrete tensile strength f_{ct} is typically neglected in modern structural concrete design in the ultimate limit state (ULS) because it is by an order of magnitude smaller than the concrete compressive strength f_c , scatters considerably, and concrete tensile failure is brittle. Moreover, relying on it might be unsafe because tensile stresses in the range of the concrete tensile strength may be present before the application of external load due to initial stresses caused by internal and external restraints, which makes the cracking load hard to predict. Nevertheless, the concrete between the cracks is subjected to tension due to the bond between reinforcement and concrete. This influences the global structural behavior and is essential for serviceability and deformation capacity aspects.¹⁻³

1.1 | RC members in tension

The complex interaction of concrete and reinforcement—with high local stress peaks at the ribs of the deformed

bars—is commonly modelled by introducing bond shear stresses τ_b , uniformly distributed along the nominal perimeter $\pi \cdot \varnothing$ of the reinforcing bar, where \varnothing = nominal bar diameter, whose magnitude is assumed to depend on the slip, that is, the relative displacement between concrete and reinforcement, or on the steel stresses.⁴⁻⁷ Typically, the behaviour is modelled using a “crack element”, that is, a reinforced concrete (RC) element between two cracks, as illustrated in Figure 1a, assuming that concrete cross-sections remain plane.

For instance, the Tension Chord model (TCM) assumes a simplified stepped, rigid-perfectly plastic bond shear stress-slip relationship, where the bond stresses depend on the steel stresses σ_s and the yield strength f_{sy} rather than the slip and are linked to the concrete tensile strength f_{ct} (Figure 1e)⁶:

$$\tau_b = \begin{cases} \tau_{b0} = 2f_{ct} & \text{for } \sigma_s \leq f_{sy} \\ \tau_{b1} = f_{ct} & \text{for } \sigma_s > f_{sy} \end{cases} \quad (1)$$

The steel strains ϵ_s and steel stresses are highest at the cracks and decrease with distance (Figure 1b,c), whereas

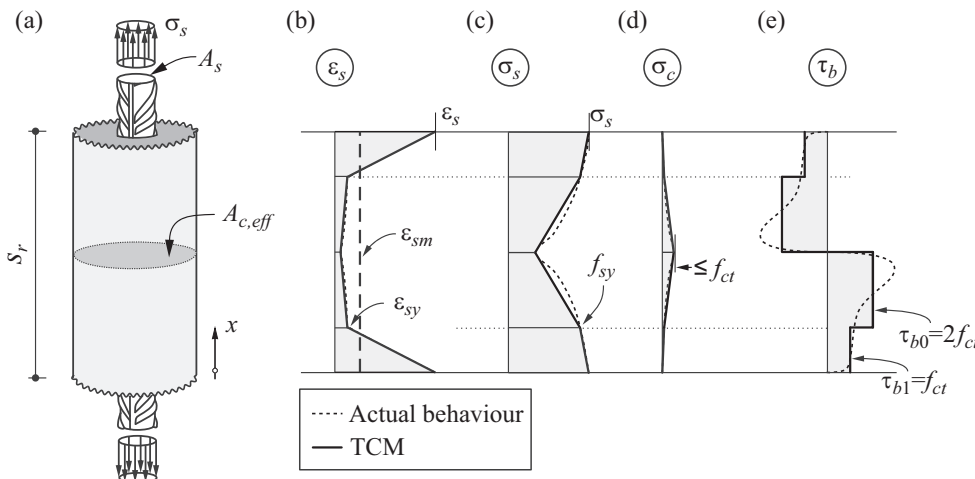


FIGURE 1 Reinforced concrete under pure tension: (a) crack element bounded by two cracks with crack spacing s_r and effective area of concrete in tension $A_{c,eff}$; (b) steel strain distribution ϵ_s ; (c) steel stress distribution σ_s ; (d) concrete tensile stress distribution σ_c , and (e) bond stress distribution τ_b for presumed actual behaviour (dashed lines) and simplified according to the tension chord model (TCM) (solid lines)

concrete tensile stresses σ_c are zero at the cracks and increase with distance (Figure 1d). For the maximum theoretical crack spacing, the concrete area $A_{c,\text{eff}}$ in the cross-section at the center between two cracks is subjected to f_{ct} . Another crack may form at this location, reducing the crack spacing to its theoretical minimum.

Since the mean reinforcement stresses are lower than the stresses σ_s at the cracks, the bonded bar, often referred to as tension chord, behaves stiffer than the bare bar, whereas the yield strength and the ultimate strength f_{su} remain unchanged since at the cracks, concrete stresses are zero. Hence, the mean strains ϵ_{sm} of the tension chord at failure are considerably smaller than those of the bare bar, even for high reinforcement ratios.⁸ Neglecting these effects, known as tension stiffening, is unsafe for ductility assessments in the ULS design, as the deformation capacity is overestimated. On the other hand, reduced mean reinforcement strains lead to smaller deformations, deflections and crack widths. Serviceability Limit State (SLS) verifications are thus beneficially affected by tension stiffening. Therefore, its consideration results in a safer, leaner, more efficient, and ultimately more sustainable design.

1.2 | Modelling of tension stiffening

Tension stiffening can be accounted for in design globally, by adopting suitably adjusted load-deformation relationships relating, for example, the applied tensile load to the average elongation of a tension chord, or the applied bending moments to the average curvature of a beam, respectively. Such global load-deformation relationships can be derived numerically by considering the local bond behaviour, defined by a bond shear stress-slip relationship, relating nominal bond shear stresses τ_b along the perimeter of the reinforcing bar to the slip between steel and concrete, as already mentioned above. Assuming a linear behaviour of concrete and reinforcement, this results in the second-order ordinary differential equation (SODE) of slipping bond, first formulated by Kuuskoski⁹ and solved by Rehm,¹⁰ and further outlined in Section 2. Depending on the assumed bond shear stress-slip relationship, solving this SODE to obtain global response predictions may be unpractical, computationally inefficient, and questionable in the light of the uncertainties and the drastic simplification of the interfacial behaviour.¹¹ This justifies further simplifications, which allow for an analytical solution of the problem (^{5,6,12-14}). Based on these assumptions, closed-form expressions for the global response are obtained. Such expressions, relating (maximum) reinforcement stresses at the cracks to mean strains, can also be obtained by semi-empirical

modifications of the stiffness of the bare reinforcement and are commonly used in design to determine crack widths and deflections.¹⁻³ Other approaches to model the tension stiffening behaviour of RC members exist. A comprehensive overview is given by Borosnyói and Balász.⁷

1.3 | Problem statement

Tension stiffening in RC beams depends highly on the effective reinforcement ratio ρ_{eff} : the ratio between the cross-sectional area of the reinforcement A_s and the effective area of concrete in tension $A_{c,\text{eff}}$. Determining $A_{c,\text{eff}}$ is straightforward in the axisymmetric case illustrated in Figure 1: if the reinforcement ratio suffices to generate through cracks before yielding, it corresponds to the concrete cross-section A_c . However, its quantification is less obvious and even controversial in more general situations. Even for the simple case of pure bending, structural design codes merely provide empirical rules based on geometrical parameters.^{1,2}

In a cross-sectional analysis (CSA), it is standard practice to assume that plane sections remain plane and normal to the beam axis x according to the Euler-Bernoulli beam theory. To account for tension stiffening, often a tension chord with a constant cross-section $A_{c,\text{eff}}$ is assumed, in which the resultant of the concrete tensile stresses F_{ct} acts at the centroid of the reinforcement. In pure bending, this results in the strains, stresses, and forces in the fully cracked cross-section II and the cross-section I at the center between two cracks shown in Figure 2a, illustrating half a crack element. The inner lever arm z and, consequently, the tensile and compressive force resultants are constant in x . In cross-section I, the concrete tensile force F_{ct} is highest, and the concrete is subjected to homogeneous tensile stresses f_{ct} over the predetermined area $A_{c,\text{eff}}$. This model is a simplification since stress redistributions between cracks may occur (Figure 2b). The inner lever arm and the force resultants generally vary between the cracks, and the centroid of the concrete tensile stress resultant F_{ct} generally does not coincide with that of the reinforcement.^{12,15}

1.4 | Overview of the present study

This study uses advanced measurement technologies to investigate these unknowns: distributed fibre optical sensing (DFOS) and digital image correlation (DIC) have emerged as suitable tools to investigate the local structural behaviour of RC elements.¹⁶⁻²⁰ Three approaches to estimate tension stiffening-related properties directly

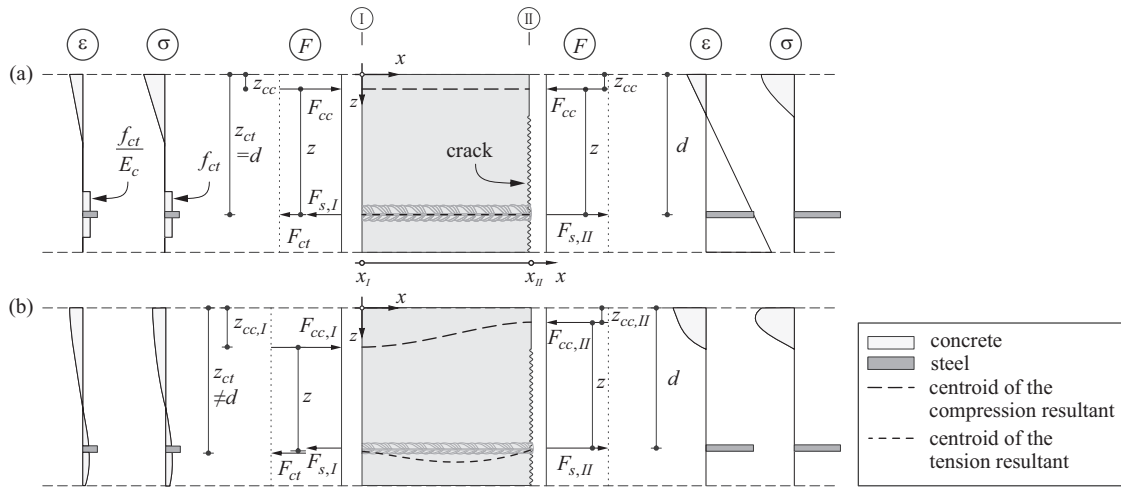


FIGURE 2 Half a crack element with centroids of force resultants (dashed lines) and strain and stress distributions in the cross-section at the center between cracks (I) and at the cracked cross-section (II): (a) as assumed by tension chord-based models and (b) for real behaviour

from DFOS and DIC measurements are presented and applied to a highly reinforced concrete beam tested in four-point bending. Selected models for the effective reinforcement ratio and the cracking behaviour for pure bending are validated against the experimental data. The presented approaches build on a first basic concept and preliminary results published by Galkovski et al.²¹ While they are not intended for application in design, the approaches are helpful to investigate the underlying physical mechanisms to reveal inconsistencies and limitations of existing models and might ultimately lead to more refined and mechanically consistent models.

2 | OVERVIEW OF CHARACTERIZATION METHODS FOR TENSION STIFFENING AND CRACKING BEHAVIOUR

Tension stiffening can be described by several equivalent (sets of) parameters, for example, (i) the concrete tensile force, (ii) mean bond stresses and the crack spacing, and (iii) mean and maximum steel and concrete strains. Any variation of the steel stresses corresponds to bond shear stresses according to the equilibrium condition of a differential reinforcing bar element:

$$\frac{d\sigma_s}{dx} = \frac{4\tau_b(x)}{\emptyset} \quad (2)$$

Combined with the assumption of linear behaviour of concrete and reinforcement, Equation (2) forms the basis for the SODE of slipping bond.

In a beam, the tension chord force $F = F_s + F_{ct}$ typically varies if shear forces V are acting, resulting in a

variable bending moment $M = F \cdot z$. However, the tension chord force may vary even if the bending moment is constant, that is, $V = 0$, since the inner lever arm z is not necessarily constant:

$$V = \frac{dM}{dx} = \frac{d(F \cdot z)}{dx} = \frac{dF}{dx} \cdot z + \frac{dz}{dx} \cdot F \quad (3)$$

$$V = 0 \rightarrow \frac{dF}{dx} \cdot z = -\frac{dz}{dx} \cdot F \quad (4)$$

Accordingly, a decrease of the steel strains, causing a reduction of F_s , need not imply an increase of F_{ct} , and vice versa. Models accounting for strain changes due to tension stiffening alone are in the following referred to as tension chord-based models, whereas equilibrium-based models additionally account for the change in z and F according to Equations (3) and (4).

Rather than $A_{c,eff}$ itself, its effects on design values are relevant to structural engineers. Therefore, the corresponding models to assess crack spacings, deformations (via mean steel strains) and crack widths are also introduced below. The study is limited to the case of short-term loading, neglecting the influence of shrinkage and creep.

2.1 | Tension chord-based models

Tension chord-based models assume the tensile force to be carried by an equivalent chord located at the depth of the reinforcement, in which both reinforcing steel and concrete tensile forces act (Figure 2a). Four models, all of them assuming a simplified bond shear stress distribution, are introduced below: The TCM (Section 2.1.1), which links the stress and the deformation states

mechanically consistently; Eurocode-2 and *fib* Model Code 2010 (Section 2.1.2), whose formulations include empirical factors accounting for the concrete cover influence; and the Compatible Stress Field Method (CSFM) (Section 2.1.3), which is based on the TCM, but adopts a generalized concept suitable to assess $A_{c,eff}$ even in discontinuity regions.

2.1.1 | Tension chord model for pure bending (Burns)

Following a proposal by Marti,²² Burns presented an approach to assess the reinforcement ratio $\rho_{eff} = A_s/A_{c,eff}$ of an equivalent tension chord (Figure 2a) for pure bending.²³ Accordingly, ρ_{eff} and hence, the effective area of concrete in tension $A_{c,eff}$, can be determined by setting the steel stresses σ_{sr} at the crack for the cracking moment M_{cr} :

$$\chi = \frac{\sigma_{sr}/E_s}{d - x_c} = \frac{M_{cr}}{EI^{II}} \rightarrow \sigma_{sr} = \frac{M_{cr}(d - x_c)E_s}{EI^{II}} \quad (5)$$

where χ = curvature; E_s =Young's modulus of reinforcement; x_c =compression zone depth determined from a fully cracked CSA; and EI^{II} =fully cracked elastic cross-sectional stiffness, equal to the steel stresses at the crack in an equivalent tension chord at crack formation:

$$\begin{aligned} \rho_{eff} \cdot A_c \cdot \sigma_{sr} &= A_c(1 - \rho_{eff} + \alpha_e \cdot \rho_{eff}) \rightarrow \sigma_{sr} \\ &= f_{ct} \left(\frac{1}{\rho_{eff}} + \alpha_e - 1 \right) \end{aligned} \quad (6)$$

where A_c = gross cross-sectional area of concrete; $\alpha_e = E_s/E_c$ modular ratio with E_c =Young's modulus of concrete, resulting in the expression:

$$\rho_{eff} = \left[\frac{M_{cr}(d - x_c)E_s}{f_{ct} \cdot EI^{II}} + 1 - \alpha_e \right]^{-1} = \frac{A_s}{A_{c,eff}} = \frac{A_s}{h_{c,eff} \cdot b} \quad (7)$$

where $h_{c,eff}$ = height of the concrete area in tension (introduced for comparison with the codes [Section 2.1.2]) and b = cross-sectional width.

Using ρ_{eff} , the TCM (or any other model based on the reinforcement ratio) can be applied analogously as for pure tension. Accordingly, the maximum theoretical crack spacing is given by:

$$s_{r0} = \frac{\emptyset \cdot f_{ct}(1 - \rho_{eff})}{2 \cdot \tau_{b0} \cdot \rho_{eff}} = \frac{\emptyset(1 - \rho_{eff})}{4 \cdot \rho_{eff}} \quad (8)$$

This corresponds to twice the distance to cause concrete tensile stresses f_{ct} over $A_{c,eff}$. Another crack may form at the center of two cracks spaced at s_{r0} . The TCM accounts for the corresponding uncertainty by introducing the crack spacing parameter $\lambda = [0.5, 1.0]$, resulting in a mean crack spacing s_{rm} :

$$s_{rm} = \lambda \cdot s_{r0} \quad (9)$$

The crack width w_{cr} , corresponding to twice the slip between concrete and reinforcement at the crack, is determined as the integral of the difference between the mean steel and concrete strains ($\varepsilon_{sm} - \varepsilon_{cm}$) over the crack spacing:

$$w_{cr} = s_{rm} \cdot (\varepsilon_{sm} - \varepsilon_{cm}) \quad (10)$$

For a bilinear stress-strain relationship of the bare reinforcement, the mean strains according to Reference 24 are given by:

$$\begin{aligned} \varepsilon_{sm} &= \frac{\sigma_s}{E_s} - \frac{\tau_{b0}s_{rm}}{E_s\emptyset} \\ &\text{for } \sigma_s \leq f_{sy} \\ \varepsilon_{sm} &= \frac{(\sigma_s - f_{sy})^2 \emptyset}{4E_{sh}\tau_{b1}s_{rm}} \cdot \left(1 - \frac{E_{sh}\tau_{b0}}{E_s\tau_{b1}} \right) + \frac{(\sigma_s - f_{sy})}{E_s} \cdot \frac{\tau_{b0}}{\tau_{b1}} \\ &\quad + \left(\varepsilon_{sy} - \frac{\tau_{b0}s_{rm}}{E_s\emptyset} \right) \\ &\text{for } f_{sy} \leq \sigma_s \leq f_{sy} + \frac{2\tau_{b1}s_{rm}}{\emptyset} \varepsilon_{sm} \\ \varepsilon_{sm} &= \frac{(\sigma_s - f_{sy})}{E_{sh}} + \left(\varepsilon_{sy} - \frac{\tau_{b1}s_{rm}}{E_{sh}\emptyset} \right) \\ &\text{for } \left(f_{sy} + \frac{2\tau_{b1}s_{rm}}{E_s\emptyset} \right) \leq \sigma_s \leq f_{su} \end{aligned} \quad (11)$$

where f_{su} = ultimate strength and E_{sh} = the strain hardening modulus of the reinforcement, respectively. Using Equation 11, the TCM is applicable in the plastic range and suitable for deformation capacity investigations.

2.1.2 | EN 1992-1-1 and *fib* Model Code 2010

Eurocode-2, that is, EN1992-1-1² (EC) and the *fib* Model Code 2010¹ (*fib*) provide semi-empirical, purely geometrical approaches for calculating crack widths, in which the crack spacing is dependent not only on the ratio \emptyset/ρ_{eff} but also on the concrete cover. Hence, the mean steel strains are not linked directly mechanically to the crack

spacing as in the TCM. The height $h_{c,eff}$ of the effective concrete area in tension for beams, slabs and members in tension, having a total height h and a static depth d , is determined by:

$$h_{c,eff} = \min \left\{ 2.5(h-d), \frac{h-x_c}{3}, \frac{h}{2} \right\} \quad (12)$$

For the crack spacing, the mean strains, and the crack widths, the readers are referenced to References 1,2.

2.1.3 | Compatible stress field method

This section introduces a concept to determine the effective concrete area in tension $A_{c,eff}$ for any element type, reinforcement configuration and loading. The approach is mechanically based but complemented by semi-empirical geometrical conditions to ensure generality. It is suitable for structural concrete elements, including static and/or geometric discontinuities and was numerically implemented in the Compatible Stress Field Method (CSFM).²⁵ The CSFM is a simplified nonlinear finite element-based continuous stress field analysis suitable for design. Simple uniaxial constitutive laws provided in standards for concrete and reinforcement are implemented, neglecting the concrete tensile strength except for tension stiffening and anchorage verifications of the reinforcing bars.

Tension stiffening, crack spacing, average reinforcement strains, and crack widths of sufficiently reinforced regions are determined using the TCM. To this end, the bilinear steel constitutive law (Equation 11) is adjusted

for each reinforcing bar to account for tension stiffening (Figure 3a). $A_{c,eff}$ is determined following four steps using the numerical methods illustrated in Figure 3b and described in the following.

Step (i) determines by equilibrium the concrete area that can be activated at f_{ct} in the extreme case of $\sigma_s = f_{su}$ for each reinforcing bar (Figure 3b). Its diameter $\varnothing_{c,eff}$ is given by:

$$\varnothing_{c,eff} = \varnothing \sqrt{f_{su}/f_{ct}} \quad (13)$$

In step (ii), symmetry conditions in y - and z -directions are applied, illustrated for reinforcing bars 3 and 4 in Figure 3b. These semi-empirical conditions are based on the findings of Frantz and Breen,²⁶ who found crack widths in beam webs to be proportional to the concrete cover of axial web reinforcement but independent of the total web width. They proposed to only account for twice the distance of the bar's centroid to the concrete surface to act in tension. In step (iii), intersecting concrete areas of adjacent reinforcing bars are attributed to the closest bar.

The resulting effective concrete area in tension of each bar after the first iteration is based on geometric considerations. Hence, this could lead to mechanical inconsistencies between close points: crack widths of neighbouring bars might differ significantly. Therefore, the condition of having identical crack spacing for proximate parallel reinforcing bars (proximity: spaced by ≤ 100 mm by default) is imposed in the last step (iv). This condition corresponds to assigning bars in proximity an identical ratio of $\varnothing(1 - \rho_{eff})/\rho_{eff} \approx \varnothing/\rho_{eff}$ (see

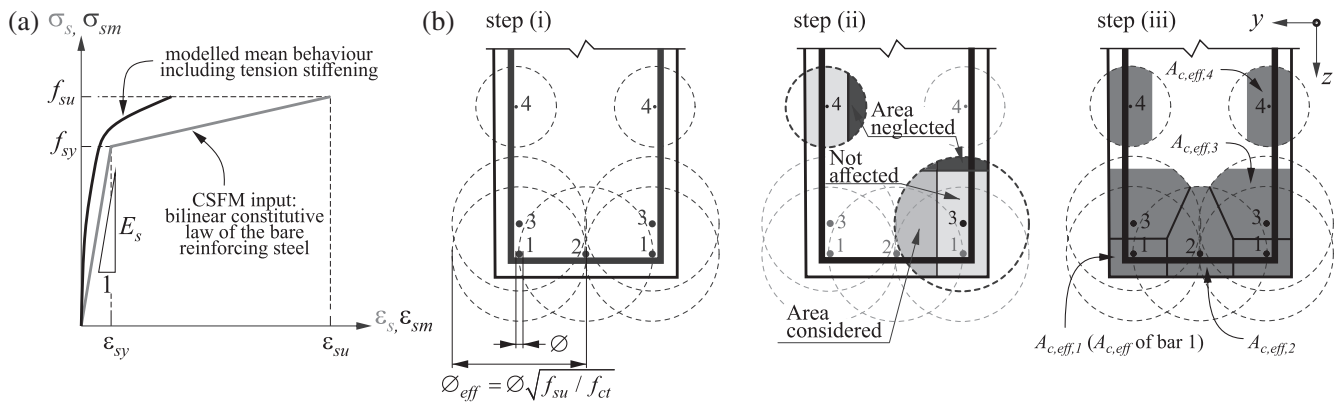


FIGURE 3 Implementation of tension stiffening in CSFM: (a) implemented increased stiffness of the bonded bar; (b) determination of $A_{c,eff}$ (stabilized cracking): (i) maximum concrete area that can be activated per bar; (ii) local symmetry condition; (iii) global geometry condition and resultant effective concrete areas. Note: Adjustment of effective concrete areas to ensure equal crack spacing of proximate bars (step (iv)) not illustrated

Equation (8)). The effective concrete area in tension for each bar i $A_{c,eff,i}$ with diameter \varnothing_i , in the proximity group with another $j - 1$ bars, is thus given by:

$$A_{c,eff,i} = A_{c,eff,max} \frac{\varnothing_i}{\varnothing_{max}} = \frac{A_{c,eff,tot}}{\sum_0^j (\varnothing_j / \varnothing_{max})} \frac{\varnothing_i}{\varnothing_{max}} = A_{c,eff,tot} \frac{\varnothing_i}{\sum_0^j \varnothing_j} \quad (14)$$

where $A_{c,eff,max}$ = effective concrete area in tension of the largest diameter bar in the proximity, \varnothing_{max} = diameter of this bar, and $A_{c,eff,tot}$ = total concrete area in tension of the proximity group. More details on CSFM can be found in Reference 25.

2.2 | Equilibrium-based approach without direct assessment of ρ_{eff} (DC)

Several researchers proposed models for the postcracking behaviour of flexural members based on equilibrium without relying on an estimation of $A_{c,eff}$.^{12,15,27–29} Based on these works, Figure 4 proposes a model based on deformation compatibility, hereafter referred to as DC.

Bond is modelled according to the TCM, and linear behaviour of concrete in tension is assumed. The outermost concrete compressive fibre's strains are assumed to decrease linearly between cross-sections II and I. Under the cracking moment $M = M_{cr}$ (Figure 4a), the concrete strains vary linearly in cross-section I, reaching a maximum of f_{ct} for the maximum crack spacing s_{r0} , and the steel strains are equal to the concrete strains at the depth of the reinforcement. In the cracked cross-section II,

concrete compressive strains are assumed to vary linearly over the depth but other than assumed in standard CSA, they are not planar with the steel strains. Instead, a linear variation of the axial displacements u_x —corresponding to the integral of axial strains between cross-sections I and II—over the depth of the cross-section is imposed, thereby ensuring plane sections remaining plane on average over a crack element²⁷.

Equation (9) applies for the mean crack spacing. With a bilinear stress–strain relationship for the bare reinforcement, the steel stresses $\sigma_{s,I}$ and $\sigma_{s,II}$ in cross-sections I and II, respectively, are related by:

$$\begin{aligned} \sigma_{s,I} &= \sigma_{s,II} - \frac{2\tau_{b0}\lambda s_{r0}}{\varnothing} \text{ for } \sigma_{s,II} \leq f_{sy} \\ \sigma_{s,I} &= \frac{2\lambda s_{r0}\tau_{b0}}{\varnothing} + \left(1 - \frac{\tau_{b0}}{\tau_{b1}}\right) (\sigma_{s,II} - f_{sy}) \\ &\text{ for } f_{sy} \leq \sigma_{s,II} \leq f_{sy} + \frac{2\tau_{b1}\lambda s_{r0}}{\varnothing} \\ \sigma_{s,I} &= \sigma_{s,II} - \frac{2\tau_{b1}\lambda s_{r0}}{\varnothing} \text{ for } f_{sy} + \frac{2\tau_{b1}\lambda s_{r0}}{\varnothing} \leq \sigma_{s,II} \end{aligned} \quad (15)$$

In a first step, the crack spacing is determined for $M = M_{cr}$ (Figure 4a) by formulating axial equilibrium in cross-sections I and II, imposing the assumed strain distributions, and the linear distribution of the axial displacements u_x over the depth of the cross-section. With $u_{x,c}$ and $u_{x,s}$ as the axial deformations of the outermost concrete fiber in compression and the reinforcement, respectively and the mean strains ϵ_{sm} given by Equation (11), it follows:

$$\frac{u_{x,c}}{x_{II}} = \frac{u_{x,s}}{d - x_{II}} \Leftrightarrow \frac{(\epsilon_{cc,II} + \epsilon_{cc,I})}{2 \cdot x_{II}} = \frac{\epsilon_{sm}}{(d - x_{II})} \quad (16)$$

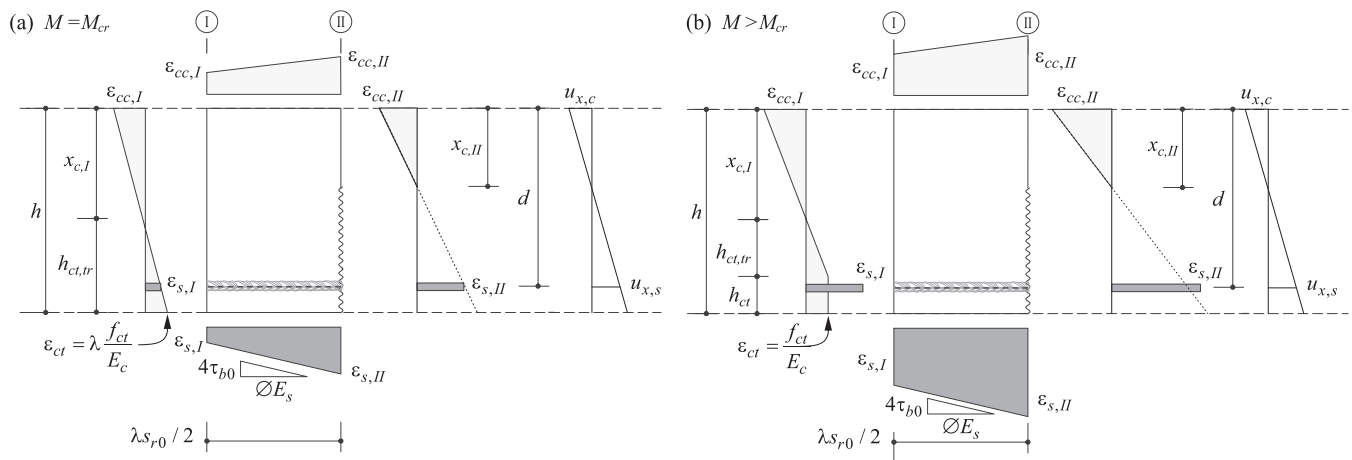


FIGURE 4 Equilibrium-based approach: Planar axial displacement u_x with assumed strain distributions for the concrete compression zone ϵ_{cc} , the tension zone ϵ_{ct} and the reinforcing steel ϵ_s in the cracked cross-section II and the cross-section at the center between two cracks I, as well as the linear variation of the steel strains and the maximum concrete compressive strain in the top fibre between both cross-sections for (a) the cracking moment and (b) higher load

The maximum crack spacing s_{r0} and the stresses and strains throughout the crack element are obtained by solving the system of equations.

When applying this model for increasing loads, keeping the crack spacing constant, concrete strains above f_{ct}/E_c might result. This has been solved either by (i) allowing concrete stresses above f_{ct} ,^{15,28,29} or (ii) considering a bilinear strain distribution in cross-section I.¹² This work assumes that concrete strains are f_{ct}/E_c over a height of h_{ct} and then decrease linearly, that is, they are decoupled from the steel strains, as shown in Figure 4b.

With the assessed crack spacing and strains, the crack widths are determined with Equation (10). Lastly, an equivalent ρ_{eff} can be defined with $h_{c,\text{eff}} = F_{ct}/(b \cdot f_{ct})$ to facilitate the comparison with the tension chord-based models, which assume an equivalent rectangular stress block with tensile stresses f_{ct} in cross-section I.

3 | DIRECT QUANTIFICATION OF TENSION STIFFENING USING FIBRE OPTIC AND DIGITAL IMAGE CORRELATION MEASUREMENTS

Advanced strain measurement techniques allow for rethinking our understanding of tension stiffening and its determination since new possibilities arise to assess, for example, (i) the concrete tensile force, (ii) mean bond stresses and the crack spacing, and (iii) mean and maximum steel and concrete strains. This section presents three possible approaches to quantify tension stiffening using distributed fibre optic sensing (DFOS) and digital image correlation (DIC).

3.1 | Advanced measurement technologies

The utilised measurement technologies are briefly presented before introducing the direct quantification methods for tension stiffening.

3.1.1 | Use of DFOS data

Instrumenting reinforcing bars with DFOS provides the steel strain distribution, and hence, maximum, minimum, and mean steel strains. Through the constitutive law, steel stresses can be determined. Local strain maxima characterize cracked cross-sections and reveal the real crack spacing s_r . Furthermore, the slip can be determined by integrating the strains from the local minima

between two cracks (cross-section I) to the cracked cross-section II, neglecting or approximating the minor concrete strains. The bond stresses at a specific location can be determined with Equation (2), that is, by equilibrium.

3.1.2 | Use of digital image correlation data

A DIC system provides full-field information of the displacements over an area of interest (AOI). The strain data of a concrete specimen's surface can be used to assess the crack behaviour (location, width and slip of cracks), for example, by using the automated crack detection and measurement (ACDM) approach.^{30,31} Moreover, concrete strains on the surface can be calculated from the measured displacements. To this end, a high-resolution system is needed to generate meaningful data. While it is possible to measure the crack behaviour of large-scale experiments with conventional DIC systems,³² the measurement of concrete compressive strains requires a high magnification to reach sufficient accuracy.¹⁶ This currently limits the field of view for sufficiently accurate concrete compressive strain measurements with 30 MPx cameras to the order of 300 mm width.

3.2 | Direct assessment of the concrete tensile force

This section presents two approaches to measure the tensile force carried by the concrete between cracks and estimate $A_{c,\text{eff}}$ and ρ_{eff} based on this by assuming a rectangular tensile stress distribution of f_{ct} . The first approach exclusively uses DFOS on reinforcing bars, the second also includes the surface concrete strain measurements from DIC.

3.2.1 | Simplified DFOS approach (FO-F)

The most straightforward approach to evaluate the concrete contribution between the cracks was proposed in Reference 21. The change in the steel force from the crack (cross-section II) to the center between cracks (cross-section I) is determined from the DFOS steel strain distribution. By equilibrium, this force change is attributed to the concrete tensile force:

$$\begin{aligned}
 F_{ct} &= \int_{x_{II}}^{x_I} (\tau_b(x) \cdot \pi \cdot \emptyset) dx = \frac{\pi \cdot \emptyset^2}{4} \int_{x_{II}}^{x_I} \frac{d\sigma_s(x)}{dx} dx \\
 &= \frac{\pi \cdot \emptyset^2}{4} [\sigma_{s,II} - \sigma_{s,I}]
 \end{aligned} \tag{17}$$

Like in tension chord-based models, the inner lever arm of forces and the total tensile and compressive force resultants are assumed to be constant.

3.2.2 | Combined fibre optical and digital image correlation-based approach

As already stated (see Figure 2 and Equations 3–4), even in the absence of shear forces, stress redistributions leading to variations of the internal lever arm z also cause steel stress variations without necessarily activating concrete in tension. Tension chord-based models neglect these variations and cannot capture the source of the steel strain change. This section presents a method, referred to as FODIC, to characterize tension stiffening from DFOS and DIC accounting for such redistributions. The approach combines concrete compressive strains obtained from DIC and steel strains from DFOS to determine F_{ct} .

Longitudinal concrete compressive strains obtained from DIC and steel strains from DFOS in cross-sections I and II (Figure 2b) are used. With appropriate constitutive laws, concrete and steel stresses and forces are derived. Formulating equilibrium in cross-section I, the tensile force F_{ct} and its position can be calculated:

$$F_{ct} + F_s + F_{cc} = 0 \quad (18)$$

$$M = F_{ct} \cdot z_{ct} + F_s \cdot d - F_{cc} \cdot z_{cc} = F_{cc} \cdot z \quad (19)$$

where z_{cc} and z_{ct} are the levers of the compressive and tensile concrete forces (see Figure 2). In cross-section II, all forces and their centroids are known from DFOS, DIC and the constitutive laws and F_{ct} is assumed to be zero. The equilibrium equations still need to be fulfilled and can be used for validation.

3.3 | Determination of tension stiffening with DFOS (FO-s)

The DFOS steel measurements can be used to obtain (i) mean bond stresses and the crack spacing, or (ii) mean and maximum steel and concrete strains (Section 3.1.1). The effective reinforcement ratio can then be determined by either the data set (i):

$$s_r = \frac{\varnothing \cdot f_{ct} \cdot (1 - \rho_{\text{eff}})}{2\tau_b \cdot \rho_{\text{eff}}} \quad (20)$$

or (ii):

$$\varepsilon_{sm} = \frac{\sigma_s}{E_s} - \frac{f_{ct} \cdot (1 - \rho_{\text{eff}})}{2 \cdot \rho_{\text{eff}} \cdot E_s} \quad (21)$$

This method still assumes a constant total tensile force, that is, neglects variations of the internal lever arm, since the equilibrium equations are derived on an equivalent tension chord.

4 | VERIFICATION OF THE METHODS WITH EXPERIMENTAL DATA

The direct quantification methods are applied to experimental data and compared with the results from the predictive approaches introduced in Section 2. Mean material parameters were used for modelling. Unless stated differently, the crack spacing parameter λ (Equation 9) is set to 0.67, which reasonably represents the average cracking behaviour.²⁵

For Burns and DC, the compression zone was modelled linearly elastic until $\varepsilon_c = 1 \text{ ‰}$, and for higher strains according to Reference 12:

$$\sigma_c = f_{cm} \left[1 - \left(\frac{\varepsilon_{cu} - \varepsilon_c}{\varepsilon_{cu}} \right)^{\lambda_c} \right] \quad (22)$$

$$\lambda_c = \frac{1}{0.1 + f_{cm}/400 \text{ MPa}}$$

where ε_{cu} = ultimate concrete strain. For *fib* and the FODIC approach, equations (7.2–10) from Reference 1 and for EC, equation (3.14) from Reference 2 were used.

4.1 | Description of the experimental program

The approaches are presented on specimen *Nn*, a beam tested in four-point bending as part of a larger experimental campaign.³³ Figure 5a presents the test setup and the geometry, Figure 5b the reinforcement layout, and Figure 5c the cross-sectional geometry and the instrumentation of both longitudinal bars. Figure 5d shows the loading history, which was divided for the analysis into seven 5 kNm load steps LS1–LS7 and the ultimate load of 37.3 kNm at LS8. The mean concrete and steel material properties are summarized in Table 1; note that the tensile strength was determined through double-punch testing.³⁴ The main reinforcement consisted of two bars with a nominal diameter $\varnothing 18$ mm, made of quenched and self-tempered (QST) reinforcing steel, as widely used today. The shear spans were reinforced with stirrups 2x5 $\varnothing 10@100$ mm. The constant bending zone excluding the supports was investigated ($x = 700\text{--}1300$ mm).

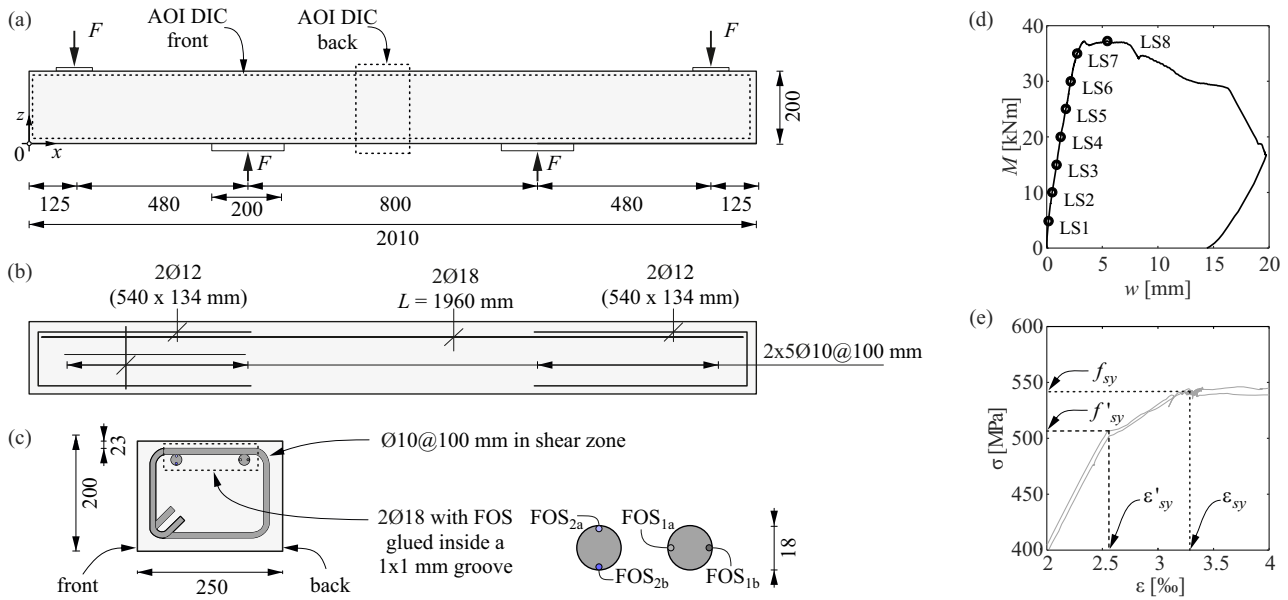


FIGURE 5 Specimen *Nn*: (a) geometry and test setup with dimensions in mm; (b) reinforcement layout; (c) geometry of the cross-section and instrumentation with fibre optical sensors (FOS) with dimensions in mm; (d) loading history against total deflections with load steps LS1 to LS8 and (e) detail of the stress–strain relationship of the QST reinforcing bars near yielding, with a yield strain and stress of the core (ϵ'_{sy} , f'_{sy}) significantly smaller than the (total) yield strain and stress (ϵ_{sy} , f_{sy})

TABLE 1 Material properties and specifications for specimen *Nn*

Material properties							
Concrete	Age [d]	Mean cylinder compressive strength f_{cm} [MPa]	Young's modulus E_{cm} [GPa]	Mean tensile strength f_{ctm} [MPa]	Maximum aggregate size D_{max} [mm]	Concrete cover c_{nom} [mm]	
	27	35.5	30.4	2.8	16	33	
Hot-rolled steel B500B (2Ø18mm)	Secant modulus E_s [GPa]	Yield strength f_{sy} (static/dynamic) [MPa]	Tensile strength f_{su} (static/dynamic) [MPa]	Yield strain of the core ϵ'_{sy} [%]	Yield strain ϵ_{sy} [%]	Hardening strain ϵ_{sh} [%]	Effective bar diameter ϕ_{eff} [mm]
	197.2	523/548	594/631	2.6	3.3	21.1	17.9

Due to the different microstructure of the more ductile ferritic-perlitic core and the higher strength martensitic outer layer,³⁵ QST reinforcing bars exhibit a nonlinear behaviour with a distinct kink at the yield strain and strength of the core (ϵ'_{sy} and f'_{sy} , respectively), before reaching the yield plateau, as illustrated in Figure 5e. This refined steel material law, including the kink, was used for all methods, that is, Equation (11) was adapted, except for the CSFM approach where a bilinear behaviour is assumed.

The main reinforcement was instrumented with two fibre optical sensors (FOS), following the best practice recommendations given in References 36,37. Bend-insensitive polyimide-coated single-mode fibers (type SM1250B3[9.8/125]P) were glued with epoxy inside

1×1 mm grooves aligned horizontally (FOS_{1a} and FOS_{1b}) and vertically (FOS_{2a} and FOS_{2b}) (see Figure 5c). The average data of both FOS of each bar are designated as FOS₁ and FOS₂, respectively. The DFOS data was acquired with the ODiSI-6104 supplied by Luna Innovations Incorporated with a resolution of 0.65 mm and 1.67 Hz.³⁸ The steel strains were postprocessed by increasing the gauge spacing to 3.25 mm and applying a moving average filter over five virtual gauges (16.25 mm), which corresponds approximately to the rib spacing, to mitigate strain peaks as an artefact due to discontinuities caused by the ribs.^{36,37}

One 3D-DIC system composed of two 28.8 MPx Allied Vision Prosilica GT6600 cameras with Quioptic Rodagon 80 mm lenses was used in the back to measure concrete

strains at a high resolution. The baseline was 350 mm and the stereo angle 20° , which resulted in an AOI of 200×150 mm (Figure 5a) and an average scale of 0.03 mm/px. The average speckle size was 0.18 mm. The correlation was carried out with the software VIC-3D (Correlated Solutions inc.²³) using a subset size of 25 px, a step size of 8 px, and a strain filter size of 9.

A second 3D-DIC system tracked the displacements and crack widths of the entire front, which was speckled manually (speckle size: 2.0 mm). This system was composed of two 12.3 MPx Flir Grasshopper 3 cameras with Quioptic MeVis 25 mm lenses, and a baseline of 1100 mm, which resulted in an average scale of 0.5 mm/px. For the correlation, a subset size of 21 px, step size of 6 px, and a strain filter size of 9 were used.

4.2 | Direct quantification methods

Figure 6 presents the results of approach FO-F for the load step LS5. The cracks on the front shown in Figure 6a were determined using ACDM; an additional crack, visible in the measurements of FOS_{1a,b} in Figure 6b, opened at about $x = 1050$ mm only at the back. The vertically aligned FOS_{2a,b} reveal pronounced local bending at the cracks with relative differences in the strains of up to 40% (Figure 6b); FOS_{2b} even measured smaller strains at the crack than between two cracks. Their average (denoted by FOS₂) does not result in equal steel strains at every crack for LS5, and neither the maxima (FOS_{2a}) nor the minima (FOS_{2b}) are the same at all cracks. The pronounced difference between FOS_{2a} and FOS_{2b} near cracks shows that the beam curvature localised at the cracks. The differences in the observed peak strains indicate that curvature localisation varied, for example, due to different crack spacings, and caused the maximum local strains (FOS_{2a}) to exceed the yield strain to a different degree at the various cracks. Determining mean steel stresses based on the measurements obtained by FOS₂ is thus challenging.

On the other hand, the average strain of the horizontally aligned sensors FOS₁ results in similar strain levels at each crack. FOS_{1a} and FOS_{1b} indicate some bending as well. This is either due to a slight misalignment, that is, not perfectly horizontal placement, or minor biaxial bending of the bar.

Using the mean stresses obtained from FOS₁ and FOS₂, respectively, bond shear stresses and the distribution of F_{ct} and h_{ct} (Figure 6c and d) are obtained according to the FO-F approach. For FOS₂, obviously wrong non-zero values of F_{ct} at the cracks result because steel stresses at the cracks differ strongly. Contrary, the method worked for FOS₁, as the bar's midplane did not yield yet.

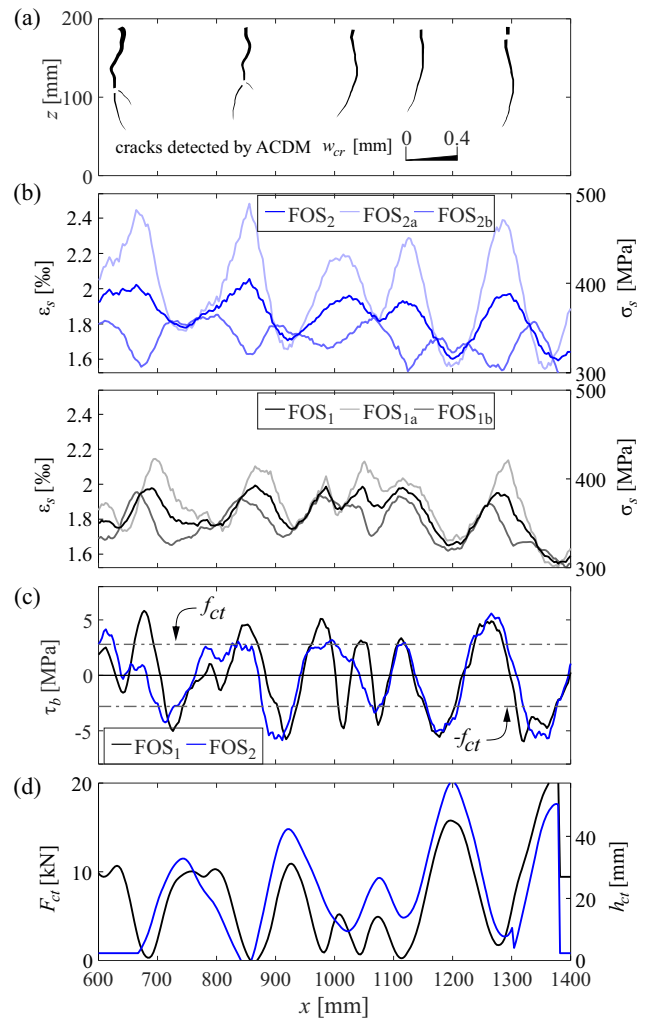


FIGURE 6 Quantification of the concrete tensile force with the FO-F approach for load step LS5: (a) crack pattern from ACDM; (b) steel strains measured with DFOS for both FOS per bar and the bar average with the stresses obtained using the steel's constitutive law; (c) bond shear stresses; (d) concrete tensile force F_{ct} and effective concrete height in tension h_{ct}

For the FODIC approach, the high-resolution 3D-DIC back system was used. Figure 7a shows the strains in x -direction ϵ_x for LS5 and the cracks detected by ACDM. The concrete strains in Cross-sections I and II were averaged over a width $dx = 16$ mm, corresponding to the maximum aggregate size. From these strains, concrete stresses were determined using the *fib* constitutive law shown in Figure 7e. The strain data of FOS₁ were used to determine the reinforcing bar stresses and forces. The resulting strains and stresses in I and II for LS1-LS8 (Figure 7b) are plausible: they (i) increase with the applied load, (ii) are smaller in I than in II, and (iii) are of reasonable magnitude. Notably, the crack on the left of cross-section I was governing, and the concrete crushing failure probably caused high strains in I at LS8.

Figure 7c compares the measured strains to those modelled by a CSA according to *fib* with and without the kink at f_{sy} . The modelled strains were slightly smaller than the measured ones for higher loads, and the onset of yielding was not well predicted.

Figure 7c shows the strains along the horizontal section cc, revealing a pronounced strain localisation in the cross-section II, with peak values exceeding 6‰. These compressive strains are significantly more concentrated in the cracked cross-section and much higher than assumed in existing models.^{12,15,28,29}

In Figure 7f,g, the derived forces are shown for LS1-8. It can be seen that in cross-section II, equilibrium is not fulfilled: the magnitude of the compression resultant F_{cc} significantly exceeds the tensile force F_s (Figure 7g). Furthermore, in some load stages, the centroid of the

concrete tensile force F_{ct} has to be located in the compression zone to satisfy equilibrium; note that F_{ct} and its centroid are sensitive to the magnitude of F_{cc} as well as the concrete stress distribution. Therefore, the results need to be critically questioned.

4.3 | Results and discussion

While the FODIC approach appears promising, it is not very straightforward. Using a conventional stress-strain relationship for concrete in compression (e.g., according to *fib*), derived from tests where average strains over a sample height of 300 mm are measured, is questionable not only in view of the results obtained here, but it is well-known that deformations localise over much shorter

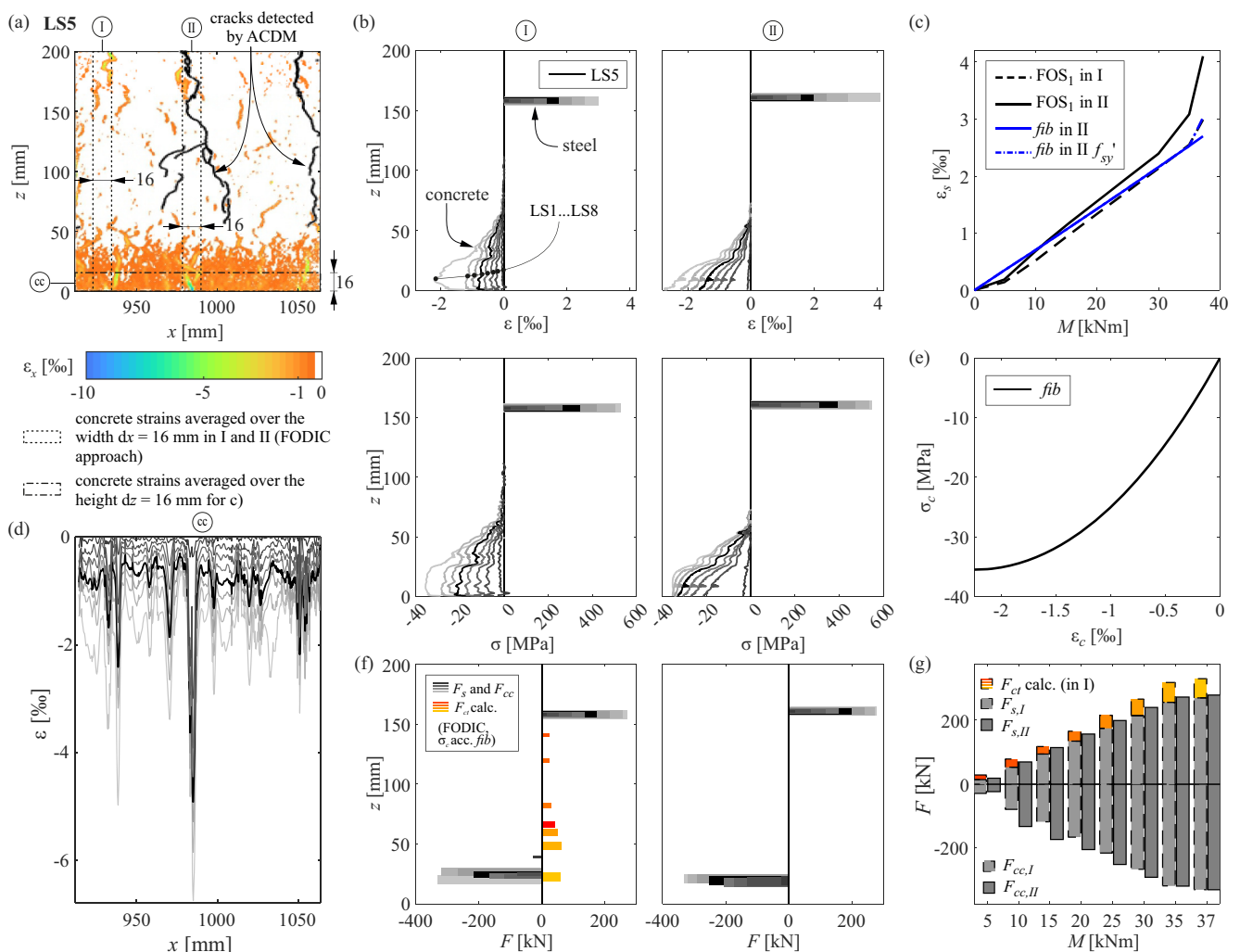


FIGURE 7 FODIC approach: (a) strains in x -direction ϵ_x for LS5, cracks detected by ACDM, and cross-sections investigated in (b) and (c); (b) strains and stresses from DFOS and DIC (FODIC) in the vertical cross-sections I (uncracked) and II (cracked) determined using (e); (c) steel strains measured (FOS₁) and predicted by CSA using (e) with and without accounting for reduced f_{sy} ; (d) strains in the horizontal cross-section cc; (e) constitutive law of concrete under compression according to the *fib* Model Code 2010; (f) FODIC compressive concrete and tensile steel forces and the calculated F_{ct} in cross-section I; and (g) magnitude of these forces in cross-sections I and II

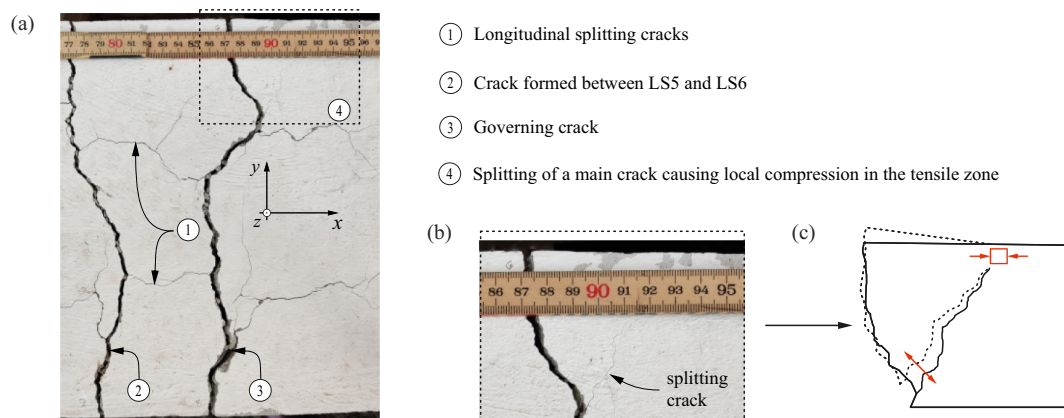


FIGURE 8 Nonuniform formation of cracks: (a) top view photograph of the crack pattern; (b) detail of top view; and (c) observed horizontal displacements of the top face

compressive fracture lengths.^{39–42} Furthermore, as illustrated in Figure 8, the choice of the representative cross-sections is challenging: cracks are neither straight, nor do they cross the bars at the same locations as they appear on the faces of the specimen (Figure 8a). To make things worse, the governing crack split close to the back face (Figure 8b), causing local compression in the tensile zone (as seen at $x = 930$ mm in Figure 7a) close to the uncracked Cross-section I, which thus may be affected. On the other hand, however, the fibre-optic sensors (e.g., FOS₁, Figure 6b) suggest that this cross-section was chosen correctly. In conclusion, the FODIC approach requires further research, and its results are excluded from the following discussion, which focuses on the other methods, that is, the tension-chord based predictive approaches by Burns (Section 2.1.1), EC and *fib* (Section 2.1.2), and CSFM (Section 2.1.3), the equilibrium-based predictive DC model (Section 2.2), as well as the direct quantification methods, FO-F (Section 3.2.1) and FO-s (Section 3.3).

Figure 9a,b compare the heights of the predicted concrete areas in tension and the effective reinforcement ratios, respectively, for the load steps LS5 (light grey) and LS7 (dark grey). The approaches FO-s and FO-F provide similar results, whereas all predictive approaches determine a higher $h_{c,eff}$. Methods DC and CSFM predict the highest $h_{c,eff}$ and, consequently, the lowest ρ_{eff} (2.5 and 3%). This suggests that a much smaller area of concrete is activated in tension in reality than predicted.

The values used for $A_{c,eff}$ and ρ_{eff} are structurally highly relevant, which is illustrated in Figure 9c–f by comparing the results of the predictive models to the experimental data. Figure 9c shows that EC and *fib* overestimate, whereas Burns and DC underestimate the crack spacing. Only CSFM predicts it satisfyingly. The mean strains (Figure 9d) are best predicted by CSFM for LS5

and LS7 and slightly underestimated by the remaining approaches. Figure 9d shows that the compression zone depth $x_{c,II}$, determined by the average position of the crack tip obtained from ACDM, is underestimated by all models. Possible explanations are, only cracks ≥ 0.05 mm are considered, and the actual cracks were thus a bit longer, or that the uncracked concrete close to the crack tip is subjected to tension.

Figure 9f,g show that EC and *fib* predicted crack widths well. However, the components contributing to this result do not match reality: the crack spacing was overestimated and mean strains were underestimated. This observation was also made in a previous study investigating a beam with a low reinforcement content.²¹ The TCM-based models underestimated the crack widths; only CSFM with $\lambda = 1$ gives satisfactory results.

The experimental crack widths increase nonlinearly from approximately 27 kNm, although the mean steel strains of FOS₁ are still smaller than the yield strength (see Figure 7d). The presumably nonlinear strain distribution of the reinforcement induced by local bending at the cracks, as implied by Figure 6, could explain this behaviour: the bars presumably already yield at their outermost edge.

Figure 9h compares the bond strength assumed by the models to the mean bond shear stress assessed by DFOS (FOS₁) in the constant bending span as explained in Section 3.1.1. The mean bond shear stresses are unexpectedly low throughout the experiment, namely on average 2.7 MPa for $M = 10$ –30 kNm, hence by a factor of at least two smaller than assumed by any of the models. After test completion, longitudinal splitting cracks could be observed at the bars, possibly explaining this (Figure 8). As all models use significantly higher bond stresses, drawing general conclusions from the results is challenging.

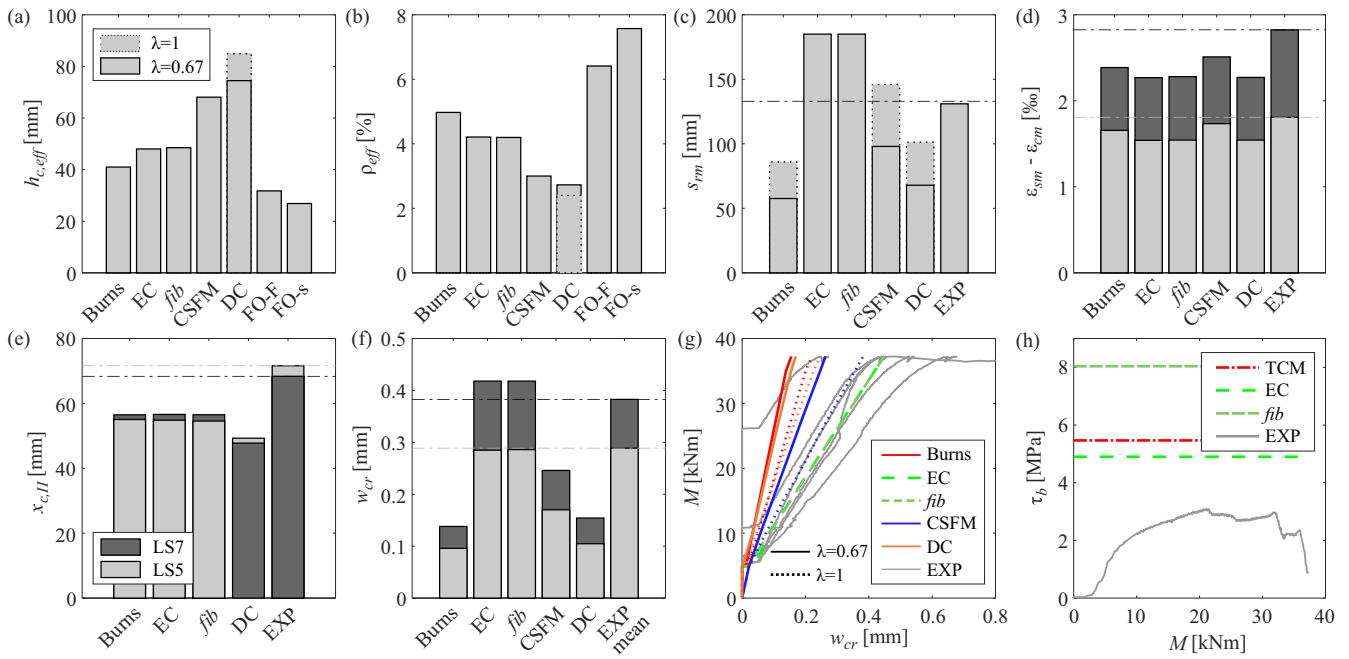


FIGURE 9 Results of the selected approaches (same order as introduced in Sections 2 and 3) compared with experimental results: (a) height of concrete in tension; (b) effective reinforcement ratio; (c) crack spacing; (d) mean strains; (e) concrete compression zone depth in cross-section II and (f) mean crack widths for LS5 (light grey) and LS7 (dark grey); (g) moment-crack width development and (h) development of mean bond stresses (determined from FOS₁) with loading

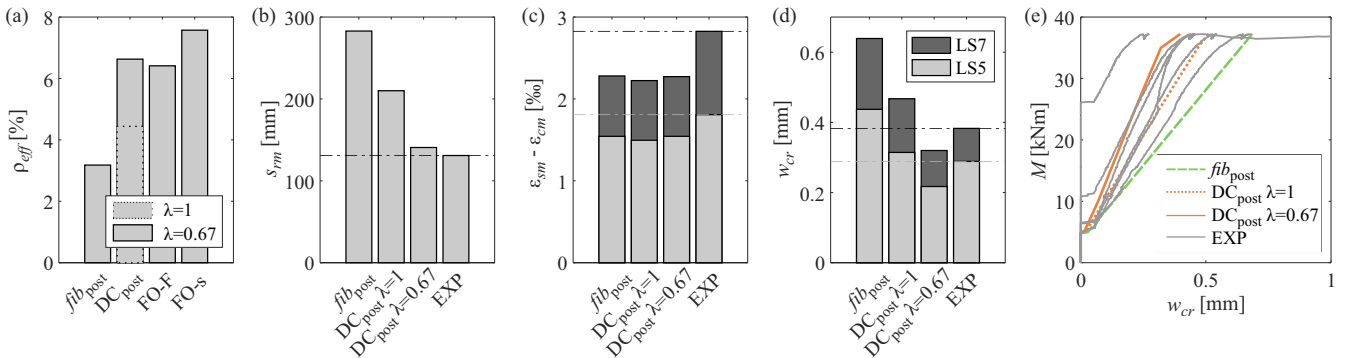


FIGURE 10 Postdiction of models *fib* (*fib_{post}*) and DC (*DC_{post}*) using the mean experimental bond stress $\tau_b = 2.7$ MPa: (a) effective reinforcement ratio, (b) crack spacing, (c) mean strains, and (d) mean crack widths for LS5 and LS7 compared with experimental data, and (e) development of crack widths with load

Therefore, Figure 10a–e present the postdiction with the models *fib* and DC (referred to as *fib_{post}* and *DC_{post}*), using the measured bond stresses (2.7 MPa) instead of the models' assumptions, that is, $1.8f_{ct}$, or $2f_{ct}$ before and f_{ct} after yielding, respectively. Using these reduced bond shear stresses, *DC_{post}* predicts the mean behaviour ($\lambda = 0.67$) very well in terms of the effective reinforcement ratio, the mean crack spacing and crack widths. In contrast, *fib_{post}* overestimates the crack spacing and crack widths by a factor of about two. The mean strains were only marginally affected. Hence, in this case, DFOS

helped identify the bond stresses and the crack spacing as the erroneous parameters.

The equilibrium-based approach DC is a suitable alternative to the Euler-Bernoulli beam theory. It is a mechanically based approach to model flexural behaviour without empirical assumptions of the effective area of concrete in tension. However, it does not provide superior predictions to the other models, for example, in terms of mean strains, presumably due to the underlying common assumption of linearly varying strains in x and z . With such assumptions, the results differ only marginally from the CSA. However,

Figure 7c shows that the common assumption of linearly varying maximum concrete compressive strains between cracks may need to be revisited since pronounced deformation concentrations occurred in the cracked cross-section.

5 | CONCLUSIONS

Selected models for assessing tension stiffening and the cracking behaviour in pure bending were validated against experimental data. Further, three novel approaches based on DFOS and DIC data are proposed to experimentally assess tension stiffening in bending. The measurement technologies help identify occurring phenomena and model deficits and, therefore, can refine the understanding of structural behaviour and improve the mechanical consistency and reliability of existing models.

DFOS identified the mean bond stresses as a significant reason for mismatching predictions. The *fib* model and the equilibrium-based approach DC were updated with the bond stresses determined by DFOS. In this position, the model based on the TCM correctly predicted tension stiffening, whereas the *fib* model worsened despite the reduced number of unknowns. Another identified weakness is that although the Eurocode-2 and the *fib* Model Code predict crack widths quite well, the crack spacing was significantly overestimated, even more with updated bond stresses.

The maximum steel stresses are essential for crack width assessment. The DFOS data revealed high local bending of the reinforcing bars at the cracks causing a stress variation of approximately 40% within the bar cross-section in the elastic state. The steel starts yielding locally before the mean bar stress reaches the yield strength, which might explain higher crack widths for loads smaller than the yield load.

The FODIC approach requires further research. The concrete tensile force determined is relatively small and prone to errors in the determined steel and concrete compressive forces. The results of advanced measurement technologies might be helpful when deriving refined constitutive laws for local material behaviour. However, the high-resolution data is demanding because it captures phenomena on a scale not dealt with by traditional structural concrete research and requires critical interpretation.

ACKNOWLEDGMENTS

The authors would like to thank Severin Haefliger and Tomislav Markić for their helpful suggestions, expertise, and fruitful discussions. Further acknowledgement goes to Patrick Bischof with whom the experimental campaign was planned and conducted and Joas Wyss, who assisted in it as part of his Master's Thesis at ETH Zurich. The

authors would also like to thank the staff of the structural engineering laboratory at ETH Zurich for their support. Open Access Funding provided by Eidgenössische Technische Hochschule Zurich.

CONFLICT OF INTEREST

The authors declare no conflict of interest.



AUTHOR CONTRIBUTIONS

Conceptualisation, Tena Galkovski, Jaime Mata-Falcón; methodology, software, validation, formal analysis, investigation, writing—original draft preparation, visualisation, project administration Tena Galkovski; writing—review and editing, Jaime Mata-Falcón, Walter Kaufmann; supervision, Jaime Mata-Falcón; funding acquisition, Walter Kaufmann. All authors have read and agreed to the published version of the manuscript.

DATA AVAILABILITY STATEMENT

The data that support the findings of this study are available from the corresponding author upon reasonable request.

ORCID

Tena Galkovski  <https://orcid.org/0000-0002-1093-4603>
 Jaime Mata-Falcón  <https://orcid.org/0000-0001-8701-4410>

REFERENCES

1. International Federation for Structural Concrete. *fib* model code for concrete structures 2010. Berlin: Ernst & Sohn; 2013.
2. EN 1992-1-1. Eurocode 2: Design of concrete structures - Part 1-1: General rules and rules for buildings', Brussels, 2004.
3. SIA. Swisscode SIA 262: concrete structures. Zurich, Switzerland: Swiss Society of Engineers and Architects (SIA); 2013.
4. Y. Goto, 'Cracks formed in concrete around deformed tension bars', *J Proc*, vol. 68, no. 4, pp. 244–251, Apr. 1971, doi: <https://doi.org/10.14359/11325>.
5. Eligehausen R. Local bond stress-slip relationships of deformed bars under generalized excitations: experimental results and analytical model. Earthquake engineering research center, College of Engineering. Berkeley, California: University of California; 1983 UCB/EERC-83/23.
6. P. Marti, M. Alvarez, W. Kaufmann, and V. Sigrist, 'Tension chord model for structural concrete', *Struct Eng Int*, vol. 8, no. 4, pp. 287–298, Nov. 1998, doi: <https://doi.org/10.2749/101686698780488875>.
7. A. Borosnyói and G. L. Balázs, 'Models for flexural cracking in concrete: the state of the art', *Struct Concr*, vol. 6, no. 2, pp. 53–62, Jun. 2005, doi: <https://doi.org/10.1680/stco.2005.6.2.53>.
8. W. Kaufmann, J. Mata-Falcón, and A. Beck, 'Future directions for research on shear in structural concrete. Towards a rational understanding of shear in beams and slabs', Lausanne, Switzerland: International Federation for Structural Concrete (*fib*); 2018.

9. V. Kuuskoski, 'Über die Haftung zwischen Beton und Stahl', Doctoral Thesis, The State Institute for Technical Research, Helsinki, 1950.
10. Rehm G. Über die Grundlagen des Verbundes zwischen Stahl und Beton. Vol Heft 138. Berlin: Verlag Wilhelm Ernst & Sohn; 1961.p. 59.
11. R. Tan, M. A. N. Hendriks, M. Geiker, and T. Kanstad, 'Analytical calculation model for predicting cracking behavior of reinforced concrete ties', *J Struct Eng*, vol. 146, no. 2, p. 04019206, Feb. 2020, doi: [https://doi.org/10.1061/\(ASCE\)ST.1943-541X.0002510](https://doi.org/10.1061/(ASCE)ST.1943-541X.0002510).
12. A. Kenel, 'Biegetragverhalten und Mindestbewehrung von Stahlbetonbauteilen', Doctoral dissertation, Institut für Baustatik und Konstruktion, ETH Zürich, 2002. doi: <https://doi.org/10.3929/ethz-a-004488185>.
13. Cantone R, Fernández Ruiz M, Muttoni A. A detailed view on the rebar-to-concrete interaction based on refined measurement techniques. *Eng Struct*. 2021;226:111332. <https://doi.org/10.1016/j.engstruct.2020.111332>
14. P. Visintin, D. J. Oehlers, and A. B. Sturm, 'Mechanics solutions for deflection and cracking in concrete', *Proc Inst Civ Eng Struct Build*, vol. 169, no. 12, pp. 912–924, Dec. 2016, doi: <https://doi.org/10.1680/jstbu.16.00009>.
15. T. Pfyl, 'Tragverhalten von Stahlfaserbeton', Doctoral thesis, ETH Zürich. [Online], 2003. <https://doi.org/10.3929/ethz-a-004502831>
16. J. Mata-Falcón, S. Haefliger, M. Lee, T. Galkovski, and N. Gehri, 'Combined application of distributed fibre optical and digital image correlation measurements to structural concrete experiments', *Eng Struct*, vol. 225, p. 111309, Dec. 2020, doi: <https://doi.org/10.1016/j.engstruct.2020.111309>.
17. S. Haefliger, J. Mata-Falcón, and W. Kaufmann, 'Application of distributed optical measurements to structural concrete experiments'. Presented at the SMAR 2017: Fourth Conference on Smart Monitoring, Assessment and Rehabilitation of Civil Structures, ETH Zurich, 2017.
18. Fernandez I, Berrocal CG, Rempling R. Long-term performance of distributed optical fiber sensors embedded in reinforced concrete beams under sustained deflection and cyclic loading. *Sensors*. 2021;21(19):6338. <https://doi.org/10.3390/s21196338>
19. Bado MF, Casas JR. A review of recent distributed optical fiber sensors applications for civil engineering structural health monitoring. *Sensors*. 2021;21(5):1818. <https://doi.org/10.3390/s21051818>
20. C. G. Berrocal, I. Fernandez, M. F. Bado, J. R. Casas, and R. Rempling, 'Assessment and visualization of performance indicators of reinforced concrete beams by distributed optical fibre sensing', *Struct Health Monit*, vol. 20, no. 6, pp. 3309–3326, Nov. 2021, doi: <https://doi.org/10.1177/1475921720984431>.
21. T. Galkovski, J. Mata-Falcón, and W. Kaufmann, 'Determination of the effective concrete area in tension relevant for modeling tension stiffening in SLS and ULS design'. In Proceedings of the fib Symposium 2021, Lisbon, Portugal, 2021, pp. 1598–1607. <https://fiblisbon2021.eventovirtual.pt/>
22. P. Marti, 'Reinforced concrete I lecture notes', Department of Civil, Environmental and Geomatic Engineering, ETH Zurich, 2004.
23. C. Burns, Serviceability analysis of reinforced concrete based on the tension chord model. ETH Zürich, 2012. doi: <https://doi.org/10.3929/ethz-a-009753066>.
24. Alvarez M. Einfluss des Verbundverhaltens auf das Verformungsvermögen von Stahlbeton. Vol 236. Basel, Switzerland: Birkhäuser; 1998.
25. W. Kaufmann *et al.*, Compatible stress field design of structural concrete: principles and validation. Zurich; Brno: ETH Zurich, Institute of Structural Engineering (IBK); IDEA StatiCa s.r.o., 2020. [Online]. <https://payhip.com/b/DP6N>
26. G. C. Frantz and J. E. Breen, 'Control of cracking on the side faces of large reinforced concrete beams', p. 262, 1978.
27. Birkenmaier M. Über Nachweise im Gebrauchszustand. *Schweizer Ingenieur und Architekt*. 1983;101(6):120–5. <https://doi.org/10.5169/SEALS-75057>
28. Markić T, Amin A, Kaufmann W, Pfyl T. Strength and deformation capacity of tension and flexural RC members containing steel fibers. *J Struct Eng*. 2020;146(5):04020069. [https://doi.org/10.1061/\(ASCE\)ST.1943-541X.0002614](https://doi.org/10.1061/(ASCE)ST.1943-541X.0002614)
29. S. Fehr, 'Trag- und Verformungsverhalten von Winkelstützmauern mit lokal korrodoerter Bewehrung', Master's thesis, Institute of Structural Engineering, ETH Zurich, 2020.
30. N. Gehri, J. Mata-Falcón, and W. Kaufmann, 'Automated crack detection and measurement based on digital image correlation', *Construct Build Mater*, vol. 256, p. 119383, Sep. 2020, doi: <https://doi.org/10.1016/j.conbuildmat.2020.119383>.
31. N. Gehri, J. Mata-Falcón, and W. Kaufmann, 'Refined extraction of crack characteristics in large-scale concrete experiments based on digital image correlation', *Eng Struct*, vol. 251, p. 113486, Jan. 2022, doi: <https://doi.org/10.1016/j.engstruct.2021.113486>.
32. A. Beck, 'Paradigms of shear in structural concrete: theoretical and experimental investigation', Doctoral Thesis, ETH Zurich, 2021. doi: <https://doi.org/10.3929/ethz-b-000482684>.
33. J. Wyss, 'Global and local analysis of UHPFRC lap splices with refined distributed optical measurements', Master's Thesis, Institute of Structural Engineering, ETH Zurich, Zurich, 2021.
34. Chen WF. Double punch test for tensile strength of concrete. *ACI J*. 1970;67(12):993–5.
35. Haefliger S, Kaufmann W. Influence of cross section loss on the stress-strain characteristics of corroded quenched and self-tempered reinforcing bars. *ConBuildMat*. 2021;282:12. <https://doi.org/10.1016/j.conbuildmat.2021.122598>
36. Galkovski T, Lemcherreq Y, Mata-Falcón J, Kaufmann W. Fundamental studies on the use of distributed fibre optical sensing on concrete and reinforcing bars. *Sensors*. 2021;21(22):7643. <https://doi.org/10.3390/s21227643>
37. Lemcherreq Y, Galkovski T, Mata-Falcón J, Kaufmann W. Application of distributed fibre optical sensing in reinforced concrete elements subjected to monotonic and cyclic loadings. *Sensors*. 2022;21.
38. 'LUNA ODiSI 6000 Data Sheet'. Luna Innovations Incorporated, 2021. [Online]. <https://lunainc.com/sites/default/files/assets/files/data-sheet/LUNA%20ODiSI%206000%20Data%20Sheet.pdf>
39. J. G. M. van Mier, 1984, 'Strain-softening of concrete under multiaxial loading conditions', Technische Hogeschool Eindhoven. [Online]. <https://www.narcis.nl/publication/RecordID/>

oai:pure.tue.nl:publications%2Fbba75bb8-d4fd-4c92-bb3d-61fe15457ab8

40. J. van Mier, 'Failure of concrete under uniaxial compression: an overview'. In *FRAMCOS-3*, 1998, vol. 2, pp. 1169–1182. <https://ci.nii.ac.jp/naid/10006091334/>
41. Lertsrisakulrat T, Watanabe K, Matsuo M, Niwa J. Experimental study on parameters in localization of concrete subjected to compression. *Doboku Gakkai Ronbunshu*. 2001;2001(669):309–21. https://doi.org/10.2208/jscej.2001.669_309
42. F. Reist, 'Druckversuche an Betonprüfkörpern mit DIC Messungen', Master's Thesis, Institute of Structural Engineering, ETH Zurich, 2016.

AUTHOR BIOGRAPHIES



Tena Galkovski, Institute of Structural Engineering, ETH Zurich, Zurich, Switzerland.
galkovski@ibk.baug.ethz.ch



Jaime Mata-Falcón, Institute of Structural Engineering, ETH Zurich, Zurich, Switzerland.
mata-falcon@ibk.baug.ethz.ch



Walter Kaufmann, Institute of Structural Engineering, ETH Zurich, Zurich, Switzerland.
kaufmann@ibk.baug.ethz.ch

How to cite this article: Galkovski T, Mata-Falcón J, Kaufmann W. Effective reinforcement ratio of RC beams: Validation of modelling assumptions with high-resolution strain data. *Structural Concrete*. 2022;23:1353–69. <https://doi.org/10.1002/suco.202100739>